Binary CoOx–SiO2 Porous Nanostructures for Catalytic CO Oxidation

Isabelle Ly, Antoine Vardon, Nicolas Chanut, Frédéric Nallet, Roland Pellenq, Mathieu Rouzières, Rodolphe Clérac, Joudia Akil, Florence Epron, Catherine Especel, et al.

ACS APPLIED NANO MATERIALS

www.acsanm.org Article

Binary CoOx–SiO_2 Porous Nanostructures for Catalytic CO Oxidation

Isabelle Ly, Antoine Vardon, Nicolas Chanut, Frédéric Nallet, Roland J.-M. Pellenq, Mathieu Rouzières, Rodolphe Clérac, Joudia Akil, Florence Epron, Catherine Especel,* and Rénal Backov*

Cite This: *ACS Appl. Nano Mater.* 2022, 5, 7331–7343 Read Online

ACCESS | Metrics & More | Article Recommendations | Supporting Information

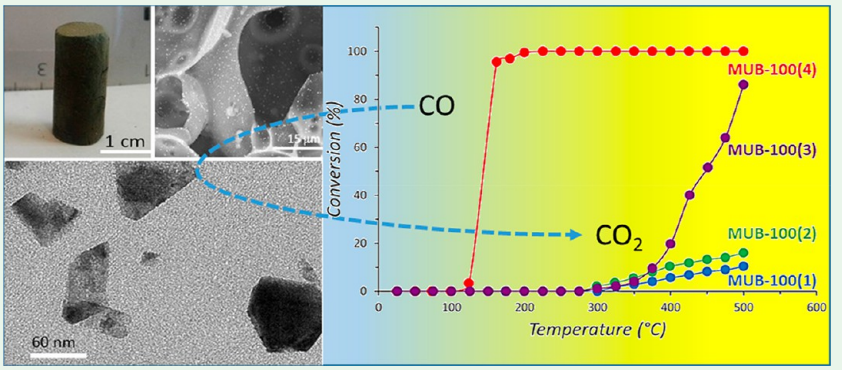

ABSTRACT: Via *integrative chemistry*, the first CoOx–SiO_2(HIPE) self-standing monoliths of cobalt nano-oxides embedded within silica macro–mesocellular hosts have been prepared. These binary CoOx–SiO_2 porous nanostructure (MUB-100(x)) materials present an average of 95% porosity. We found out that high cobalt concentration maintains the hexagonal-2D organization of the mesoscopic voids when applying the thermal treatment at 700 °C. Their specific surface areas fall between 400 and 500 $m^2\ g^{-1}$ when assessed by Ar physisorption measurements. At the microscopic length scale, as revealed through magnetic investigations, the low cobalt content foams MUB-100(1) and MUB-100(2) are made of the amorphous β-$Co(OH)_2$ phase coexisting with the silica network, whereas increasing the cobalt concentration during the one-pot syntheses (MUB-100(3) and MUB-(4) materials) favors the formation of the spinel Co_3O_4 and olivine Co_2SiO_4 crystalline nanoparticles embedded within silica. When considering the CO oxidation catalytic performance, the MUB-100(4) is able to totally convert the CO flow before 200 °C (starting at 125 °C) while achieving 50% conversion for a light-off temperature (T_{50}) of 145 °C, revealing the good efficiency of the MUB-100(4) in CO oxidation with which up to 4 catalytic cycles have been performed without disrupting drastically the catalytic performance and reaching thermodynamic stability from cycle 2 to cycle 4.

KEYWORDS: *chimie douce, multiscale open-cell scaffolds, CO oxidation, integrative chemistry, contact catalysis*

1. INTRODUCTION

Polymerization/polycondensation of concentrated biliquid foams and washing out the discontinuous hydrophobic phase employed as a soft mold provide solid macrocellular foams. Silverstein recently reviewed various synthetic routes for these systems[1,2] while addressing a complete "contemporary contemplation" of the scope. The network precursors being organic can be varied on demand, thus offering a real "holy grail"[3] when turning toward solely organic poly(HIPE) (HIPE = high internal phase emulsion).[4] When looking at inorganic porous media, this synthetic path is based on synergistic templating scenarios combining (i) lyotrope liquid crystals (concentrated micelles), inducing mesoporosity (pore diameters ranging from 2 to 50 nm); (ii) concentrated oil-in-water biliquid foams (direct emulsions) promoting the connected macroscopic voids (pore diameters above 50 nm); and (iii) the hydrolytic sol–gel process that condenses the continuous aqueous phase.[5] As the inorganic skeleton is made of amorphous silica, the microporosity (pore diameters below 2 nm) relies on the voids emerging from the SiO_4 tetrahedron statistical repartition. These self-standing foams are labeled Si(HIPE),[5] and they can be further hybridized to specify applications toward contact catalysis.[6−9] For example, when considering an inorganic mix of titania and silica, porous materials have been recently designed and employed within the fields of random lasing[10−12] or toward CO_2 photoreduction in volume.[13] In addition, we were also able to associate silica and alumina, inducing highly efficient acidic heterogeneous

Received: March 22, 2022
Accepted: April 18, 2022
Published: May 2, 2022

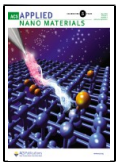

catalysts.[14] Despite these results, there is still a lack of research dedicated to inorganic-HIPE in comparison with the field of organic polyHIPE. This reduced attention results from tendency of the inorganic synthetic path to shrink the inorganic skeleton through both intrinsic polycondensation and applied thermal treatment. Additionally, drying the monolith has to hamper capillary forces. As such, obtaining inorganic self-standing monolithic materials is not such an easy task to achieve. Despite this drawback, we have recently generated SBA15-Si(HIPE) materials being both 2D-hexagonal mesoporous and monolithic while leveraging a chaotrope−kosmotrope salt effect.[15,16] In addition, there are also strong research efforts to generate novel mixed-nano-oxides-inorganic-foams from the HIPE process considering the full periodic table because, like ceramics, they are resilient to both solvent and temperature while maintaining high surface area when considering the nanoscale. They are thus outstanding candidates for liquid or gaseous phase heterogeneous catalysis. Particularly, the heterogeneous oxidation of CO is nowadays the most efficient gas exhaust remediation process where almost all the commercial catalysts make use of noble metals because of their high activity for CO oxidation and stability.[17−23] However, it is well-known that the major drawbacks of noble metals are their scarcity and associated high and increasing cost.[17,24] Consequently, several studies have been reported on the development of non-noble transition metal-based catalysts for CO oxidation,[17,25−30] where cobalt oxides, Co_3O_4 especially, represent promising candidates.[17,31] In this vein, we are proposing the design of the first CoOx−SiO_2(HIPE) multiscale porous monolithic MUB-100 materials (MUB stands for "Materials of the University of Bordeaux")[32] and present their characterization and specific applications as highly efficient heterogeneous catalysts toward CO oxidation.

2. EXPERIMENTAL SECTION

2.1. Catalyst Syntheses. High-purity dodecane (≥99%), hydrochloric acid 37 wt % (HCl), tetraethylorthosilicate (≥99%, TEOS), and cobalt(II) chloride hexahydrate $CoCl_2{\cdot}6H_2O$ were purchased from Sigma-Aldrich. Tetradecyltrimethylammonium bromide (TTAB) was supplied by Alfa Aesar, while dichloromethane (CH_2Cl_2, ACS-reagent RPE) was purchased from Carlo Erba. All the chemicals were used as received without any further purification. Deionized water was obtained using a Milli-Q water purification system. $CoCl_2{\cdot}6H_2O$ (3.255, 1.713, 0.571, or 0.2852 g) were dissolved in 16 g of a TTAB (35 wt %) water solution. Then 5 g of HCl (37 wt %) was added prior to adding 5 g of TEOS (pH below 0.05). The solution was stirred for 10 min to both promote TEOS full hydrolysis and evaporate the native EtOH molecules. Then, 37 g of dodecane was emulsified drop by drop under manual stirring. The native direct oil-in-water biliquid foam was transferred into several hemolysis test tubes employed as canisters, where the sol−gel process is advanced for 1 week at 25 °C. Then, the solidified emulsions were extracted from the canister and washed for 12 h in dichloromethane (CH_2Cl_2). The native materials were dried in a desiccator for 1 week, followed with a second 3 days of drying in air. Finally, a thermal treatment was applied to the materials following the same conditions as presented in the literature.[32] Final micro−meso−macroporous monoliths are labeled MUB-100(1), MUB-100(2), MUB-100(3), and MUB-100(4), indicating an increasing amount of cobalt employed for the syntheses (Table 1). Final materials are shown in Figure 1.

2.2. Material Characterizations. *2.2.1. Scanning Electron Microscopy.* The samples were prepared and observed through the same procedure presented in ref 32.

2.2.2. X-ray Diffraction. X-ray diffraction (XRD) patterns were obtained using a PANalitycal X'pert MPD-PRO Bragg−Brentano $\theta-\theta$ geometry diffractometer equipped with a secondary monochromator and an X'celerator detector over an angular range of 2θ = 8−80°. Each acquisition lasted for 6 h 47 min. The Cu Kα radiation was generated at 45 kV and 40 mA (λ = 0.15418 nm). The samples were prepared on a silicon wafer "zero background" sample holder and flattened with a piece of glass.

2.2.3. Small-Angle X-ray Scattering. X-ray scattering experiments were performed under the same conditions as reported in ref 32.

2.2.4. Transmission Electron Microscopy−Transmission Electron Diffraction (TEM−TED). TEM samples were prepared and observed in the same conditions as reported in ref 32.

The diffraction patterns were generated with a TEM FEI Talos F200S 200 kV. Regarding the coupled TEM−TED investigations, image acquisitions followed the procedure reported in ref 32.

2.2.5. Magnetism Measurements. The magnetic susceptibility measurements were performed using a PPMS-Evercool II Quantum Design magnetometer with a VSM module operating between 1.9 and 300 K for applied dc fields ranging from −9 to 9 T. Measurements were done on ground samples (12.63, 8.17, 9.41, and 8.33 mg for MUB-100(1), MUB-100(2), MUB-100(3), and MUB-100(4), respectively), which were loaded into a sealed polyethylene bag (typically 25 mg). For MUB-100(1), MUB-100(2), MUB-100(3), and MUB-100(4), the field dependence of the magnetization was measured at 100 K to verify the absence of significant ferromagnetic impurities. The magnetic susceptibility was measured in the 2−300 K range at 0.1 T. Field dependence of the magnetization up to 9 T was measured at 2, 3, 5, and 8 K, and a complete hysteresis loop was done at 2 K (at 0.2 T/min). Zero-field-cooled (ZFC)−field-cooled (FC) experiments were done between 2 and 100 K by measuring the magnetization as a function of temperature at 0.4 K/min (i) cooling the sample in zero dc field to 2 K, then (ii) measuring from 2 to 100 K in a dc field of 50 Oe, and finally (iii) measuring from 100 to 2 K in the same applied dc field of 50 Oe. The magnetic data were corrected for the sample holder and the intrinsic diamagnetic contributions. The SiO_2/HIPE-based precursor was measured and, as expected, was found to be diamagnetic (-0.65×10^{-6} cm^3/g or -39×10^{-6} cm^3/mol) with negligible paramagnetic impurities (less than 0.5% of an S = 1/2 spin). The linearity of the magnetization in the field at 100 K indicates also the absence of significant ferromagnetic impurities.

2.2.6. Mercury Intrusion Porosimetry (MIP). Intrusion/extrusion mercury measurements were performed under the conditions presented in ref 32.

2.2.7. Thermogravimetric Analysis (TGA). TGA was performed in air using a TGA 5500 Discovery TA apparatus. The heating ramp was set to 5 °C min^{-1} with a first temperature ramp from 25 to 180 °C. We then imposed a temperature plateau of 6 h at 180 °C followed with a temperature ramp from 180 to 700 °C; the final temperature is maintained for 6 h. The decreasing temperature is uncontrolled and governed by the oven inertia.

2.2.8. Temperature-Programmed Reduction (TPR) Experiments. TPR investigations were done over the MUB-100 materials in order to assess the reducibility of their oxide phases. Prior to performing the TPR, the catalysts were pretreated *in situ* under inert flow (Ar) for 1 h at 200 °C and cooled to 30 °C. The TPR experiments were performed with a 10 vol % H_2/Ar gas mixture (30 mL·min^{-1}). The temperature range was 30−500 °C with a ramp of 10 °C·min^{-1}, and the temperature was then maintained at 500 °C for 1 h. The measurements of the H_2 consumption were made in an AutoChem II/Micromeritics apparatus, using a thermal conductivity detector.

2.2.9. Elemental Analyses. Elemental analyses have been performed through ICP while using both ICP AES iCAP 6500 DUO and ICP AES iCAP 7400 Radia apparatus.

2.3. Quantitative Porosity Investigation. *2.3.1. Gas Physisorption Experiments.* The physisorption measurements followed the same procedure as that presented in ref 32 while using a Micromeritics 3Flex surface characterization analyzer (Micromeritics Instrument Corp, Norcross, GA).

2.3.2. Helium Pycnometry. Materials skeleton densities have been determined through the same procedure and apparatus as described in ref 32.

https://doi.org/10.1021/acsanm.2c01258
ACS Appl. Nano Mater. 2022, 5, 7331−7343

Scheme 1. Whole Synthetic Steps Occurring for the MUB-100(x) Series Generation

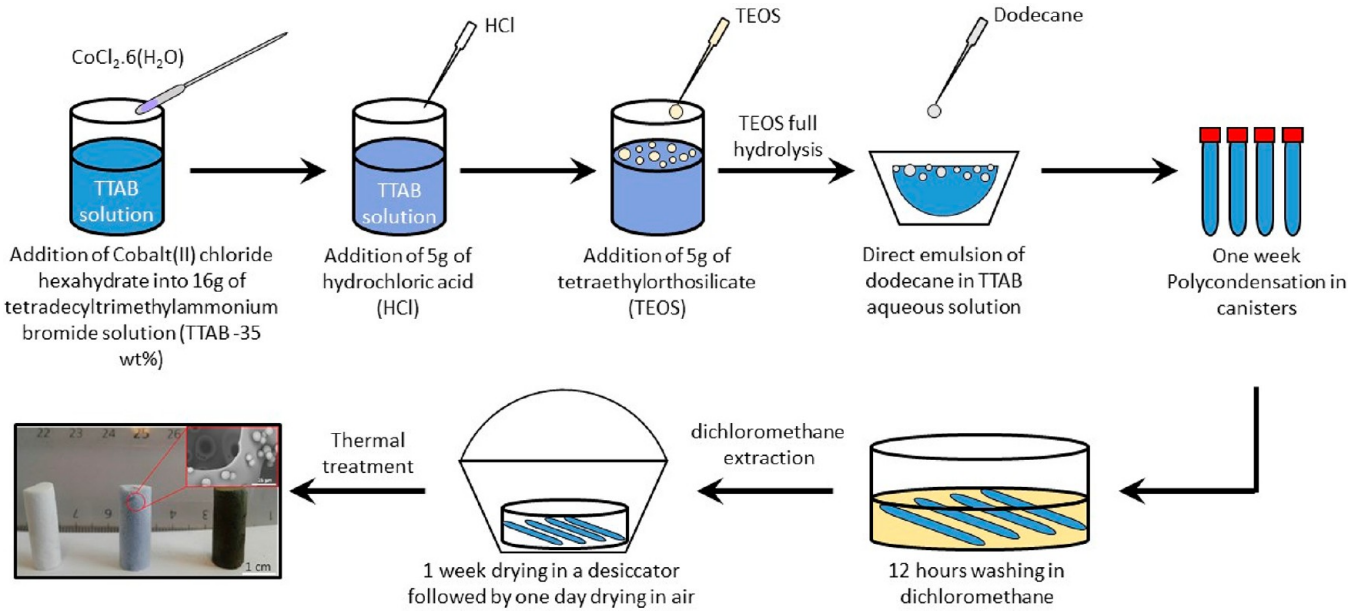

Table 1. Elemental Analyses and TGA Addressing Materials' Molar Weight (MW) and Stoichiometry

sample	Co wt % found	Co wt % calc	Si wt % found	Si wt % calc	H_2O wt % found[a]	H_2O wt % calc	MW ($g \cdot mol^{-1}$)	proposed stoichiometry
MUB-100(1)	0.62	0.62	37.2	36.7	11.2	11.1	76.50	$(Co(OH)_2)_{0.008}(SiO_{1.6}(OH)_{0.8})_{1.0} \cdot 0.47H_2O$
MUB-100(2)	1.41	1.46	37.5	36.7	10.0	9.9	76.62	$(Co(OH)_2)_{0.019}(SiO_{1.6}(OH)_{0.8})_{1.0} \cdot 0.42H_2O$
MUB-100(3)	3.23	3.10	34.3	35.0	10.9	11.2	80.18	$(Co(OH)_2)_{0.038}(Co_3O_4)_{0.0012}(Co_2SiO_4)_{0.0003}(SiO_{1.6}(OH)_{0.8})_1 \cdot 0.5H_2O$
MUB-100(4)	10.1	9.9	31.6	31.0	12.0	11.7	90.93	$(Co(OH)_2)_{0.038}(Co_3O_4)_{0.035}(Co_2SiO_4)_{0.005}(SiO_{1.6}(OH)_{0.8})_1 \cdot 0.59H_2O$

[a]The H_2O wt % values have been found by TGA under air under a heating rate of 5 °C/min. The TGA can be found within the Supporting Information (Figure S1). Elemental analyses have been performed using ICP for cobalt and silicon atoms wt % quantifications.

2.4. Catalytic Experiments. The catalytic activity toward the CO oxidation was performed by using a fixed bed tubular reactor containing 50 mg of the crushed sample. The reactor was continuously fed with a gas flow constituted by 11.6 mL/min of CO and 29.0 mL/min of O_2, balanced with N_2 (total flow rate = 100 mL/min), corresponding to a CO/O_2 ratio equal to 0.4 and a weight hourly space velocity (WHSV) of 120 000 $L \cdot h^{-1} \cdot kg^{-1}$. The reactor was put in a tubular furnace with a temperature controller, allowing the reaction temperature to be gradually increased (temperature ramp: 5 °C/min), with steps of 25 °C. The effluents at the reactor outlet were analyzed on line under steady-state conditions in a Varian gas chromatograph (GC-3800) equipped with a thermal conductivity detector (TCD) (the temperatures applied for the injector, oven, and detector were 150, 50, and 120 °C, respectively). Before the catalytic test, the sample was activated for 2 h under an O_2-N_2 mixture (respective flow rate of 29.0 and 59.4 mL/min) at 500 °C under a 10 °C/min temperature ramp.

3. RESULTS AND DISCUSSION

The whole process of obtaining the MUB-100(x) series is depicted in Scheme 1. Considering the whole process, the most time-consuming step is the drying one, where concomitant capillary forces have to be circumvented as much as possible. That is the reason why a slow drying process in a desiccator is first performed. Avoiding this step induces uncontrolled shrinkage of the gel when drying, and the final monolithic character is lost. In addition, we should note that the sol–gel process is occurring under acidic conditions (pH placed below 0.05, below the silica isoelectric point of pH 2.1) where the silica precursors are positively charged. This feature is indeed important to explain the cobalt nano-oxide structure revealed through XRD investigations and discussed later.

3.1. Macroscopic Scale Description of the Materials. When considering Figure 1a,b, we can notice that the MUB-100 series are self-standing monoliths whatever the amount of cobalt introduced during the syntheses, as is the case with traditional cobalt-free Si(HIPE) final materials.[5] Upon increasing the cobalt content (Table 1), the color of final materials varies from pale blue to dark brownish, being the sign of Co_3O_4 presence in this last case, as we will see later when characterizing the materials at the microscopic length scale.

When performing SEM observations, typical aggregated hollow spheres (polydisperse in sizes)[5] depicting the foams' macroporosity (Figure 1c-h), where internal cellular junctions can be observed (Figure 1d,f,h) indicating thus an open porosity. This macroporosity arises from the dodecane oily phase removal through the CH_2Cl_2 washing process. Aside the macroscopic cell observation, EDS investigations have been performed to assess the cobalt dispersion within the foams at the macroscopic scale (Figure 1k–n). The general information is that whatever the cobalt concentration (Table1), the cobalt is homogeneously dispersed at the macroscale. As expected, the cobalt densities over EDS spectra are more pronounced when the cobalt concentration increases from MUB-100(1) to MUB-100(4). As such, we can see the high density of tiny crystals at the macroscopic wall surface for the MUB-100(4)

https://doi.org/10.1021/acsanm.2c01258
ACS Appl. Nano Mater. 2022, 5, 7331–7343

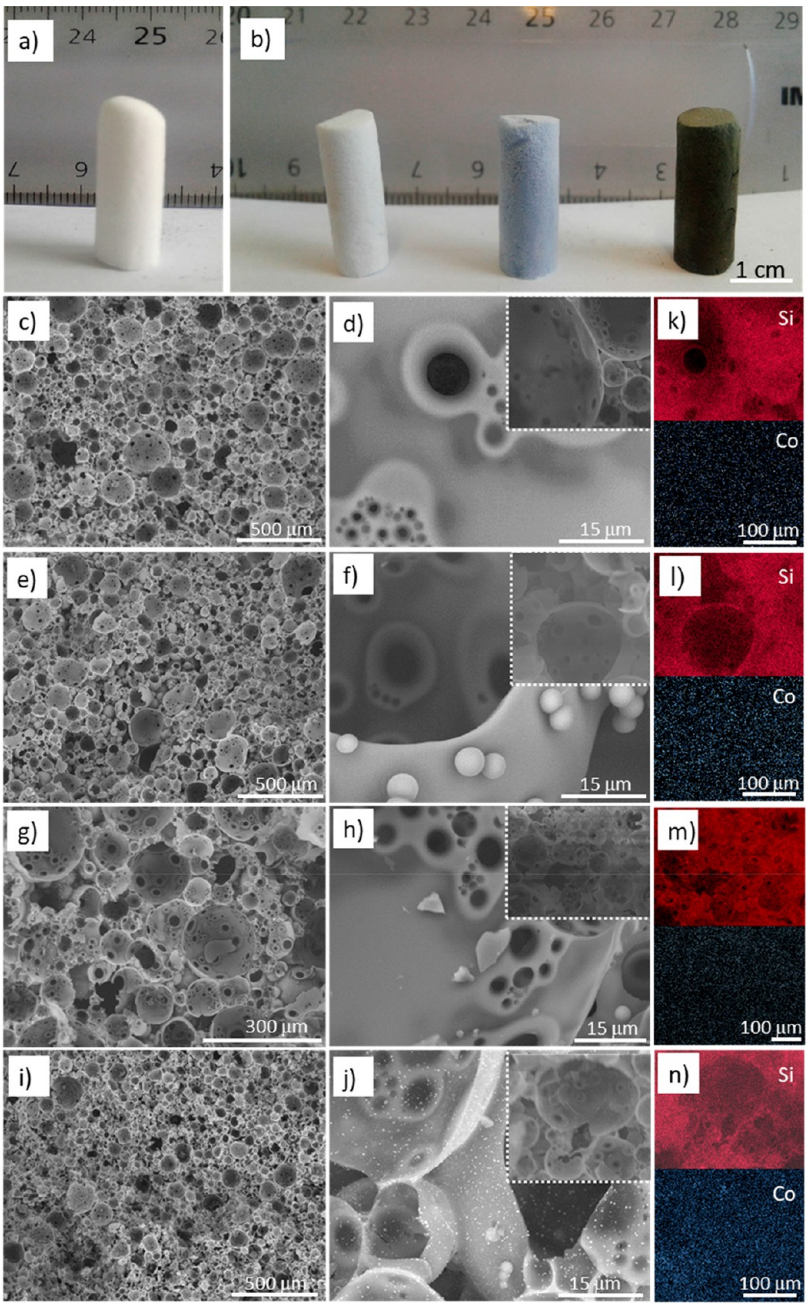

Figure 1. MUB-100 materials SEM observation. (a) Traditional silica-based HIPE (Si(HIPE)) and (b, from left to right) MUB-100(1), MUB-100(2), and MUB-(4) where the cobalt amount is increasing. (c–j) SEM images: (c and d) MUB-100(1), (e and f) MUB-100(2), (g and h) MUB-100(3), (i and j) MUB (4). (k–n) EDS images: (k) MUB-100(1), (l) MUB-100(2), (m) MUB-100(3), (n) MUB-100(4). The spent areas for EDS are the ones inset in the top right corners of panels d, f, h, and j.

(Figure 1j), which are not visible when considering the MUB-100(1), MUB-100(2), and MUB-(3) materials (Figure 1d,f,h).

Beyond these qualitative data, the porosity of the MUB-100 materials has been evaluated by combining mercury intrusion porosimetry (MIP), which determines both the macrosopic voids' connecting windows (Figure 2) and bulk density (Table 2), with helium (He) pycnometry addressing the determination of the skeleton density (Table 2). The percentage of porosity has been determined through eq 1:

$$\%\ \text{porosity} = [1 - (\text{bulk density}/\text{skeleton density})] \times 100 \quad (1)$$

with porosity in percent and the bulk and skeleton densities in $g{\cdot}cm^{-3}$ (see Table 2).

We first underline that the pore size distributions (Figure 2) are the ones corresponding to the windows that restrict the mercury infiltration. Therefore, the connecting cell junctions, which can be seen in Figure 1d,f,h,j, play a key role in this experiment, in contrast with the macroscopic cells themselves. As is the case for Si(HIPE) materials,[5,15,16] the cell-connecting throats are rather polydisperse from 15 to 0.1 μm while expressing a bimodal character, which is clearer for the MUB-100(4). Beyond the cell junction sizes, mercury porosimetry, in combination with He pycnometry, allows for the determination of the porosities and bulk densities (Table 2).

https://doi.org/10.1021/acsanm.2c01258
ACS Appl. Nano Mater. 2022, 5, 7331–7343

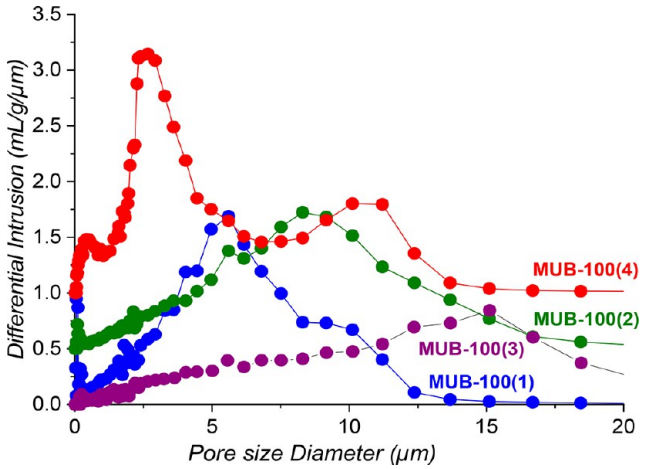

Figure 2. MIP pore size distribution. MUB-100(1), blue dots; MUB-100(2), green dots; MUB-100(3), purple dots; MUB-100(4), red dots. To improve clarity, the MUB-100(2) and the MUB-100(4) profiles were shifted upward by 0.5 and 1.0 mL/g/μm, respectively.

Table 2. Bulk Density Determined by MIP, Skeleton Density Measured by Helium Pycnometry, and Calculated Porosity Following Equation 1[a]

sample	porosity (%)	skeleton density ($g \cdot cm^{-3}$)	bulk density ($g\ cm^{-3}$)
Si(HIPE)	96 ± 2%	2.22 ± 0.01	0.085 ± 0.005
MUB-100(1)	96 ± 2%	2.42 ± 0.01	0.089 ± 0.005
MUB-100(2)	96 ± 2%	2.56 ± 0.01	0.087 ± 0.005
MUB-100(3)	97 ± 2%	2.53 ± 0.01	0.083 ± 0.005
MUB-100(4)	97 ± 2%	2.60 ± 0.01	0.083 ± 0.005

[a]The Si(HIPE) data are extracted from ref 32.

As shown in Table 2, we can see that MUB-100(x) materials synthesized are highly porous, with an average porosity of 96%. Upon increasing the cobalt content, a minor increase in the skeleton density with a disruption for the MUB-100(3) compound can be observed, while the bulk density remains constant in the limits of the error bars. The singularity of the MUB-100(3) material is discussed further with the Ar and N_2 physisorption measurements.

3.2. Mesoscopic Scale Description of the Materials. To get insights regarding the mesoscale porosity of the MUB-100(x) series, argon adsorption at 87 K and nitrogen adsorption at 77 K have been performed for the determination of their surface area (Figure 3). All isotherms depict adsorption at low relative pressure highlighting the microporosity, and a hysteresis loop at higher relative pressure (gas capillarity condensation), more or less pronounced depending on the sample, indicates the presence of mesoporosity. We can note a slight increase of the volume adsorbed for the adsorption isotherms at high relative pressure that announces the solid foams' macroporosity. As addressed in Table 3, we can see that BET surface areas are systematically lower when using Ar over N_2.

This can be explained by the quadrupolar nature of the N_2 molecules, which is responsible for the intimate interaction with surface functional groups and therefore the reason for the observed apparent surface area increase. This effect is even more visible when looking at the microporous surface area (Table 3). Besides affecting the orientation of the N_2 molecules, these interactions strongly correlate with the

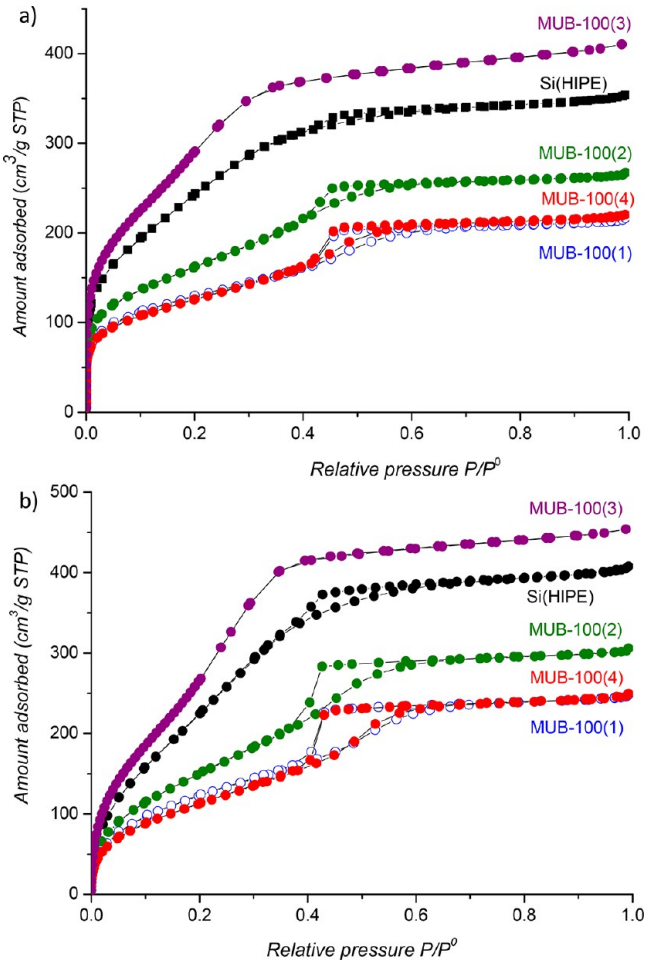

Figure 3. Gas physisorption measurements: (a) N_2 adsorption−desorption curves and (b) Ar adsorption−desorption curves. MUB-100(1), blue circles; MUB-100(2), green dots; MUB-100(3), purple dots; and MUB-100(4), red dots. The Si(HIPE) curves are extracted from ref 32.

micropore filling pressure, so that the pore filling pressure is not clearly correlated with the pore size. In contrast to N_2, Ar does not exhibit specific interactions with surface functional groups, favoring thus a much more accurate surface area determination for samples presenting functional surface groups. Thus, for these reasons and based on the recommendations reported in the IUPAC technical report of 2015 dedicated to gas physisorption, the results obtained with Ar will be also discussed in this work. We can note that both micro- and mesoscopic surface areas reached via Ar physisorption investigations drastically decrease from the Si(HIPE) to the MUB-100 series with the exception of the MUB-100(3) material where the surface areas appear slightly higher than that of the Si-(HIPE) and almost double when compared with their MUB-100(x) homologues.

At first glance, we can say that the decrease of surface area is totally expected as we introduce β-$Co(OH)_2$, Co_3O_4, or Co_2SiO_4, which are intrinsically denser than SiO_2. As the silica wt % decreases, all the micro- and mesoporosity associated with silica also decrease, being less representative of the whole material's porosity. This explanation is valid only if the silica intrinsic porosity remains constant while varying the cobalt content. In more detail, we can note that the microporosity decreases from 271 to 113 $m^2\ g^{-1}$ when going from Si(HIPE)

https://doi.org/10.1021/acsanm.2c01258
ACS Appl. Nano Mater. 2022, 5, 7331−7343

Table 3. N_2 and Ar Surface Area Determinations[a]

sample	N_2-BET ($m^2 \cdot g^{-1}$)	Ar-BET ($m^2 \cdot g^{-1}$)	S_{micro} (N_2) ($m^2 \cdot g^{-1}$)	S_{meso} (N_2) ($m^2 \cdot g^{-1}$)	S_{micro} (Ar) ($m^2 \cdot g^{-1}$)	S_{meso} (Ar) ($m^2 \cdot g^{-1}$)
Si(HIPE)	930	874	425	505	271	603
MUB-100(1)	450	413	180	270	113	300
MUB-100(2)	584	530	195	389	57	473
MUB-100(3)	988	912	383	605	152	912
MUB-100(4)	439	387	133	306	31	356

[a]The values obtained for the cobalt free Si(HIPE) foam are extracted from ref 32.

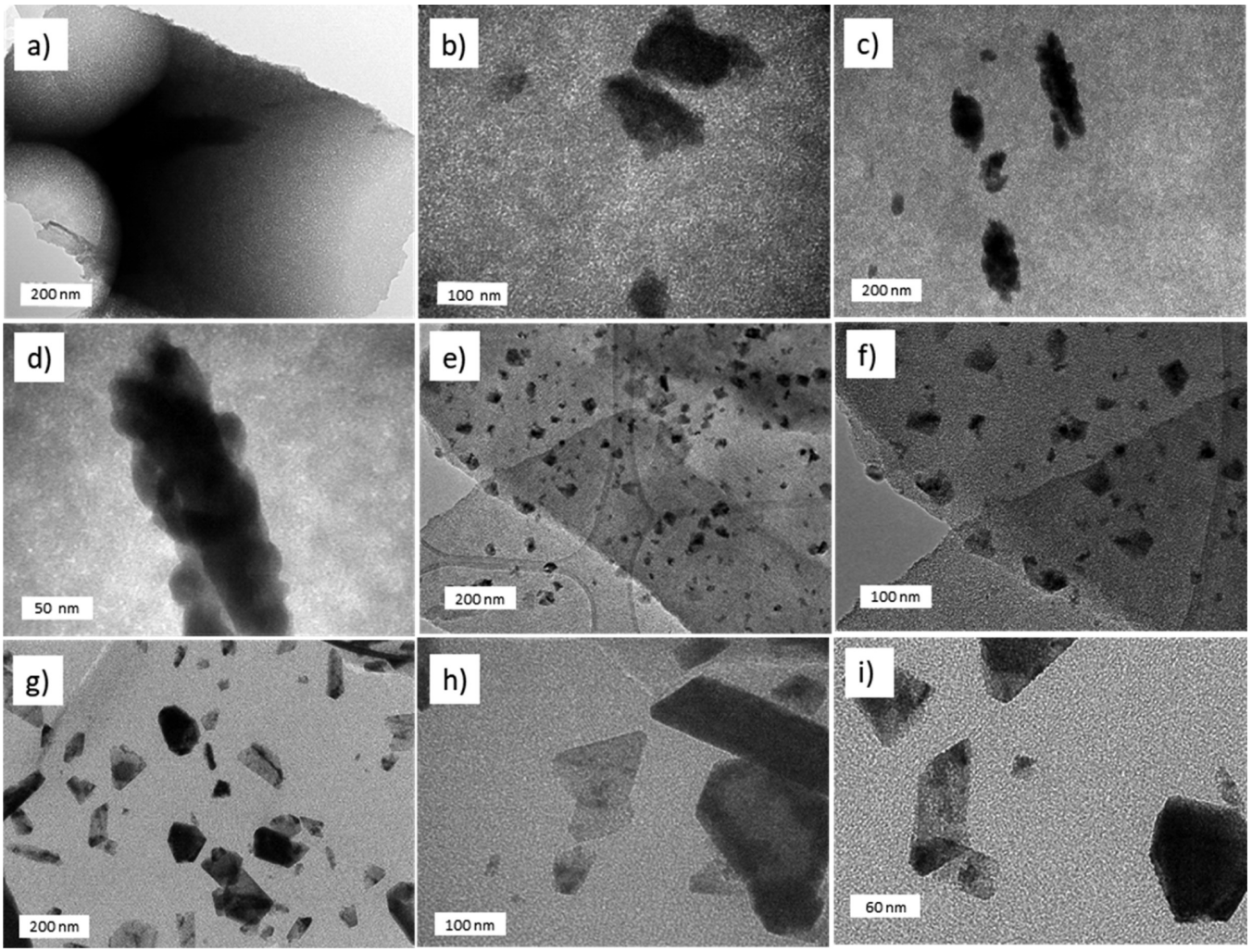

Figure 4. TEM observations. (a and b) MUB-100(1), (c and d) MUB-100(2), (e and f) MUB-100(3), and (g–i) MUB-100(4).

to MUB-100(1), respectively (Table 3), while the latter bears only 0.62 wt % cobalt, that is, 8.0×10^{-3} cobalt atoms per SiO_4 tetrahedron when considering its stoichiometry (Table 1). One may argue that this decrease of microporosity is due to the increase of the skeleton density combined with some cobalt "oxo" and/or "hydroxo" clusters trapped within the inter-SiO_4 tetrahedron microporosity, thereby minimizing its accessibility. Additionally, it has been demonstrated that the addition of Sr^{2+} or Ba^{2+} during the sol–gel-induced epitaxial growth of SiO_2 onto oriented silicon wafer favors "devitrification", that is, both higher packing density and organization of the SiO_4 tetrahedrons within the geometrical space, leading to α-quartz nucleation and growth instead of amorphous silica.[33] We may not exclude this "partial" process here where Co^{2+} may enhance the overall SiO_4 packing density during the polycondensation, without going here to the full devitrification scenario upon calcination treatment. This highest SiO_4 packing density may also intrinsically limit the MUB-100 microporosity, being lower in the case of the MUB-100(3). Still focusing on the Ar physisorption data, we can see that the MUB-100(2) material bears a higher mesoscopic surface area, in comparison to the MUB-100(1), despite bearing more β-$Co(OH)_2$. The tendency is the same when comparing the MUB-100(2) and MUB-100(3) materials where mesoscopic surface areas increase upon increasing the cobalt content. This behavior involves a "salting out" effect of the cobalt salt over the lyotrope mesophases, as discussed later in the text. Of course, this effect is also present for the MUB-100(4), but in that case the increase of the mesoscopic voids does not compensate any longer the increase of cobalt oxide content

https://doi.org/10.1021/acsanm.2c01258
ACS Appl. Nano Mater. 2022, 5, 7331–7343

where the Co wt % goes from 1.46 to 9.90 (Table 1), resulting in a lower mesoscopic specific surface area expressed per gram of sample. Considering the mesoscopic surface areas, the MUB-100(3) materials seem to provide the optimum configuration in which both higher siliceous mesoscopic surface area is generated through a salting out effect and additional surface area emerges from the higher amount of cobalt oxide nanoparticles (Figure 4e,f).

To address further the characterization at the mesoscopic length scale, we performed TEM local investigations (Figure 4). We can note that for MUB-100(1) (Figure 4a,b), MUB-100(2) (Figure 4b,c), and MUB-100(3) (Figure 4e,f) some aggregates appear without a specific shape over mesoporous walls bearing locally a vermicular character. We intended to perform transmission electron diffraction (TED) measurements over these aggregates, which unfortunately do not diffract, while considering solely the MUB-100(1) and MUB-100(2).

Considering the silica structure, poorly organized vermicular mesoscopic voids, characteristic of traditional Si(HIPE),[5] are observed. With MUB-100(4), the configuration seen through TEM is rather different. First, we can notice very distinct and well-shaped nanocrystals are polydisperse in size (10−300 nm) (Figure 4h,i). The second main difference relies on the mesoscopic void distribution that, in addition to the vermicular mesophase, is rather more organized and present in the vicinity of the nanocrystals (Figure 4h,i) where hexagonal-2D organization can be locally observed. At this stage, we have to address the driving force of the coexistence of this local hexagonal 2D void organization. Without cobalt and at the same TTAB and TEOS concentrations and pH, the hexagonal 2D phase obtained here is solely vermicular, as with traditional Si(HIPE) materials.[5] Two parameters may be claimed to address this difference. First, the solvent in use in this study to wash the precalcined materials is no longer THF[5] but CH_2Cl_2. The latter, being poorly miscible with water, will not lixiviate the tension-active molecules, thereby favoring the 2D-hexagonal organization characteristic of high TTAB concentrations.

The second explanation may rely on a cobalt chloride salt that provides a salting out effect[34] toward the lyotropic mesophase, decreasing the surfactant solubility in water. As salt concentration increases, the "salting out" effect will promote surfactant aggregation and thereby a denser configuration while reaching an organized hexagonal-2D structure. This observation agrees with the results reported by Dag et al.[35] and our previous results[15,16] when dealing with the generation of mesoporous silica particles, or SBA15-Si(HIPE) prepared from either the coassembly of CTAB and P123 or only P123. In this latter report, it has been demonstrated that the mesoporous ordering is favored while increasing the salt content. Here, we specify that whatever the salt content, the Debye length falls always around 0.3 nm because of the presence of oxonium (H_3O^+) electrolytes (pH is placed below 0.05 with HCl, below the silica isoelectric point at pH 2.1),[36] thus avoiding a possible electrostatic screening scenario involving the MUB-100 mesoporosity ordering. A third explanation of this hexagonal-2D organization present at the vicinity of the cobalt oxide crystals (Figure 4g,h) would be a pseudoepitaxial effect in which the crystallization of the Co_3O_4 crystals during the thermal treatment will promote higher organization of the silica network at their vicinity. However, this explanation may be disregarded after establishing that the hexagonal-2D organization of the mesoscopic structure exists prior to the thermal treatment as evidenced from small-angle X-ray scattering (SAXS) of the precalcined materials (Figure S2). Coming back to calcined materials, SAXS indicates the structural description observed by TEM. As depicted in Figure 5a, the smaller wave-vector part of the scattering intensity data displays, at the notable exception of the MUB-100(4) sample, the power-law decay through the exponent −4 (Porod's law)[37] describing a clear-cut interface separating an "outer" empty medium (air) from an "inner" filled medium (silica). The

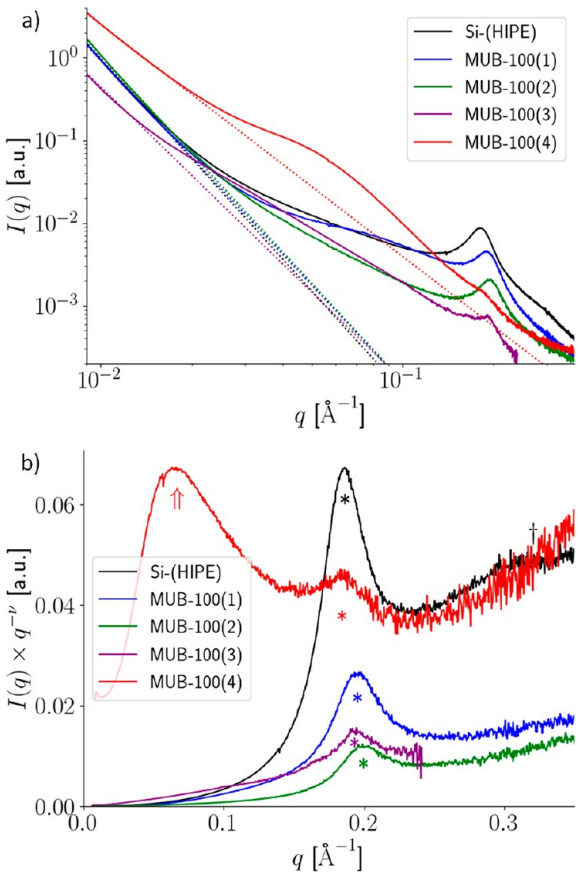

Figure 5. (a) SAXS intensities (double logarithmic scale) for the reference Si-(HIPE) sample (black, data extracted from ref 32) and the three MUB-100(1) (blue), MUB-100(2) (green), MUB-100(3) (purple), and MUB-100(4) (red) samples. The colored dotted lines represent power-law decaying intensities with exponents close to −4 (Porod's law) except for the MUB-100(4) sample where the exponent is found to be close to −3. (b) SAXS Porod-like representation for calcined materials, highlighting the meso-structure of the reference Si-(HIPE) sample (black), and of the three MUB-100(1) (blue), MUB-100(2) (green), MUB-100(3) (purple), and MUB-100(4) (red) samples (ν is close to −4 as expected from Porod's law, except for the MUB-100(4) sample where its value is found to be close to −3). The colored star marks the q* location in reciprocal space of the characteristic structural peak arising from the 2D hexagonal phase used for the synthesis. Considering the reference Si-(HIPE) sample a "second-order" peak may be found at roughly $\sqrt{3}$ the "first-order" peak (dagger symbol)—as expected for hexagonal 2D order. Associated structural parameters (derived from $2\pi/q^*$): Si-(HIPE), 3.38 nm; MUB-100(1), 3.21 nm; MUB-100(2), 3.14 nm; MUB-100(3), 3.24 nm; and MUB-100(4), 3.40 nm. Note the presence at about $2\pi/100$ Å^{-1} (upward double arrow symbol), and for MUB-100(4) only, of a broad feature possibly associated with Co_3O_4 nanocrystals. The Si (HIPE) curves are extracted from ref 32.

https://doi.org/10.1021/acsanm.2c01258
ACS Appl. Nano Mater. 2022, 5, 7331−7343

significant discrepancy from Porod's law observed for the MUB-100(4) with a decay following a power-law with exponent −3, associated with a broad feature at small angles (ca. 0.06 $Å^{-1}$), is credited to the cobalt-rich nanocrystals segregated from the siliceous continuous phase, as indicated by TEM investigations (Figure 4g,h). The diffraction peak associated with the hexagonal-2D organization of the mesoscopic structure (Figure 5a,b) is always found at larger angles for the calcined materials, which are particularly obvious when considering the Porod depiction of Figure 5b. The calcination also obviously increases disorder (compare to Figure S2, in which the so-called "second-order" peak is less pronounced or absent) in addition to making the structure more compact. Another important point to address is the fact that for the MUB-100(4) and despite a synthetic Si/Co molar ratio of 0.57 the Co_3O_4 crystal sizes remain at the nanoscopic length scale, reaching 200−300 nm at most (Figure 4g).

This trend is certainly due to the synthetic sol−gel acidic condition where the silica network will bear a strong fractal character[36] rather than Euclidean. As such, the silica network fractal character will show high specific surface area where the Co_3O_4 nucleation enthalpy will be minimized, favoring the nucleation events toward the crystal growth, thereby minimizing their sizes. This feature is of importance when dealing with heterogeneous catalysis, as we will see later.

3.3. Microscopic Scale Characterization of the Materials. We first used X-ray diffraction (XRD) to address the cobalt oxide phases existing within the MUB-100 series (Figure 6).

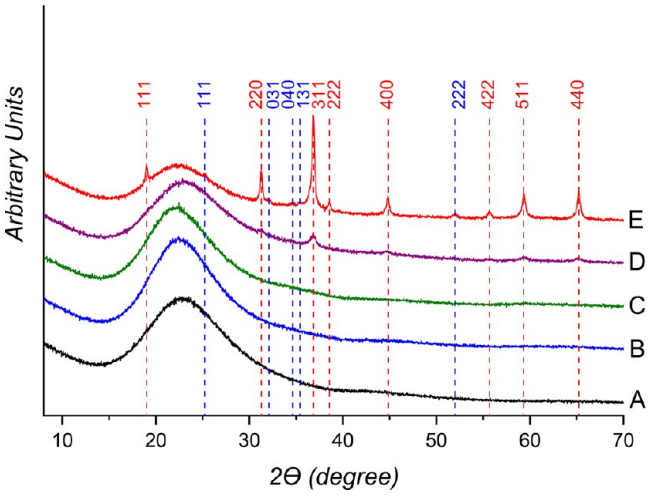

Figure 6. XRD investigations: (A) Si(HIPE) sample (black), (B) MUB-100(1) (blue), (C) MUB-100(2) (green), (D) MUB-100(3) (purple), and (E) MUB-100(4) (red). Red dashed lines at (111), (220), (311), (222), (400), (422), (511), and (440) are the main Bragg diffraction peaks of the Co_3O_4 cubic phase (JCPDS card no. 74-1657). Blue dashed lines at (111), (031), (040), (131), and (222) are the main diffraction peaks that correspond to the Co_2SiO_4 olivine phase (JCPDS card no. 84-1298).

We can notice that for the MUB-100(1) and MUB-100(2) materials there are no Bragg peaks, in agreement with the TED investigations. We can observe only a broad hump centered at 23−24° (2Θ) that corresponds to the amorphous silica network (statistical repartition of the SiO_4 tetrahedron).[5] Considering the MUB-100(3), XRD assesses the presence of spinel Co_3O_4 (Figure 6D). We have performed TEM−TED (Figure S3) that shows additionally the presence of Co_2SiO_4 nanostructures. For the MUB-100(4), XRD investigations evidence the presence of a biphasic system made of Co_3O_4 and Co_2SiO_4 (Figure 6E), meaning that the Co_2SiO_4 phase is growing while increasing the cobalt content. Unfortunately, both XRD and TEM/TED investigations were unsuccessful (no Bragg peaks detected) for the MUB-100(2) and MUB-100(1) materials. Considering the pale blue color of the MUB-100(1) monolith (Figure 1b), we first intuited that the phase present was amorphous Co_2SiO_4,[38] but this phase is normally appearing only above 1100 °C when addressing acidic based syntheses,[38] while the thermal treatment applied here is reaching a maximum temperature of 700 °C. To get the spinel Co_2SiO_4 at relatively low temperature, the synthetic path should be addressed under alkaline conditions (above the silica isoelectric point) where the Co^{2+} species will have molecular affinity with the negatively charged silicate precursors.[39] In the present cases, the Co_2SiO_4 phase appears only above 3 wt % of Co (Table 1 and Figure 6), certainly for the Co^{2+} species to be concentrated highly enough to both circumvent phase separation between positively charge siliceous precursors and the Co^{2+} and optimize the Co thermal diffusion when the thermal treatment is applied. In contrast, at low cobalt wt %, the phase separation between siliceous precursor and silica is effective during the sol−gel synthetic step, while providing the β-$Co(OH)_2$ embedded within the siliceous host when the thermal treatment is applied. As the β-$Co(OH)_2$ phase is amorphous, we have decided to run magnetic susceptibility (χ) experiments to collect more information on the chemical structure of the MUB-100(1) and MUB-100(2), which present a lower cobalt content. As such, magnetic properties of the MUB-100(1) and MUB-100(2) materials have been studied using dc susceptibility measurements. In agreement with a paramagnetic behavior, the temperature dependence of the reciprocal susceptibility ($1/\chi$) is linear above 50 K for the two materials. They can be fitted to a Curie−Weiss law ($\chi_{CW} = C/(T - \theta)$) with Curie constants of C = 0.0287 and 0.0656 cm^3 K mol^{-1} and Weiss temperature of θ = +7.6 and +5.6 K for MUB-100(1) and MUB-100(2), respectively (left part of Figure S4). Considering these positive Weiss constants, ferromagnetic interactions are dominant in these materials like the bulk β-$Co(OH)_2$ phase, which displays an antiferromagnetic order below 12.3 K.[40,41] Curie constants are consistent with the expected amount of S = 3/2 Co^{2+} centers. When normalized for one S = 3/2 Co^{2+} center, the Curie constants are 3.59 and 3.45 cm^3 K mol^{-1} for MUB-100(1) and MUB-100(2), respectively, which correspond to large g factors of 2.77 and 2.71 expected for S = 3/2 Co^{2+} systems.[42] Above 100 K and in agreement with the $1/\chi$ versus T data, the χT products for MUB-100(1) and MUB-100(2) are almost constant with the above estimated Curie constants (right part of Figure S4). At lower temperatures, the χT product increases and shows a clear maximum around 8.2 K confirming the presence of dominant ferromagnetic interactions. Zero-field-cooled (ZFC)−field-cooled (FC) experiments have been performed below 100 K (left part of Figure S5). A bifurcation of the ZFC/FC data is observed below 5 K, indicating the presence of magnetic bistability likely associated with surface effects of β-$Co(OH)_2$ nanoparticles and the blocking of the magnetization (with a blocking temperature T_B around 3.8 at 0.4 K/min).[40] The field dependence of the magnetization (M) at 2 K confirms the presence of a magnetic bistability (hysteresis) as shown in the right part of Figure S5. At 9 T,

https://doi.org/10.1021/acsanm.2c01258
ACS Appl. Nano Mater. 2022, 5, 7331−7343

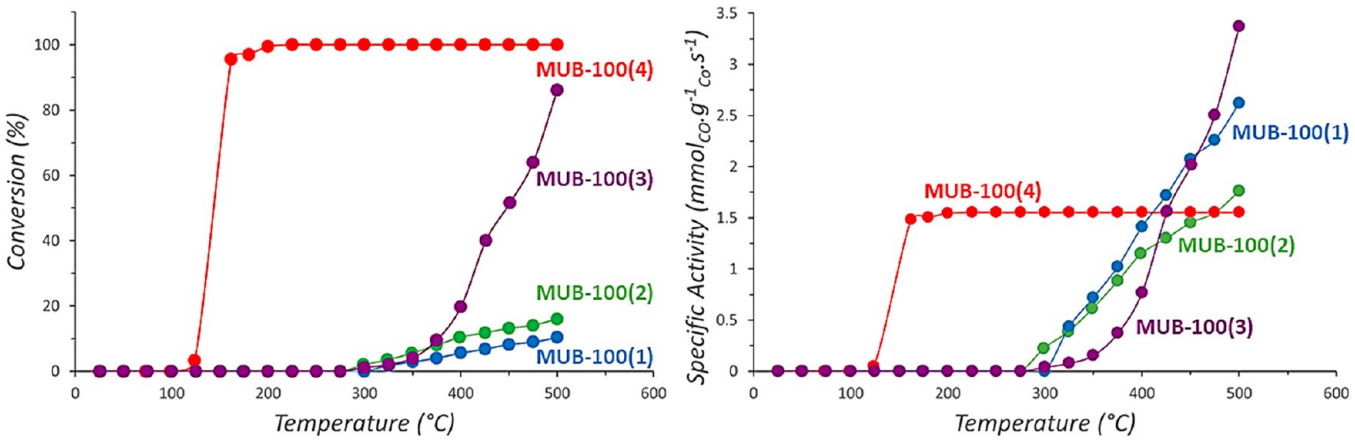

Figure 7. Left: CO conversion (%) vs temperature for MUB-100(1) (blue dots), MUB-100(2) (green dots), MUB-100(3) (purple dots), and MUB-100(4) (red dots). Right: Specific activity vs temperature for MUB-100(1) (blue dots), MUB-100(2) (green dots), MUB-100(3) (purple dots), and MUB-100(4) (red dots).

the magnetization is almost saturated to 0.0205 and 0.0549 μ_B for MUB-100(1) and MUB-100(2), respectively. These values correspond to 2.6 and 2.9 μ_B per Co^{2+} ions in agreement with the presence of a large Co^{2+} zero-field splitting, which induces a marked decrease of the magnetic moment. At 2 K, the remnant magnetizations are 0.0036 and 0.0083 μ_B with associated coercive fields of 870 and 710 Oe for MUB-100(1) and MUB-100(2) (at 0.2 T/min), respectively. Overall, the magnetic properties of the MUB-100(1) and MUB-100(2) materials are consistent with their respective chemical composition (Table 1) and the presence of superparamagnetic β-$Co(OH)_2$ nanoparticles as already described in the literature.[40,41] For MUB-100(4), the $1/\chi$ versus T plot is also linear above 50 K, which can be fitted to a Curie−Weiss law with C = 0.284 cm^3 K mol^{-1} and θ = −13.8 K (left part of Figure S4). As for MUB-100(1) and MUB-100(2), this material is paramagnetic, but in this case, dominant antiferromagnetic (AF) interactions between spin carriers are detected as expected in the presence of bulk Co_3O_4.[42] On the basis of the chemical composition (Table 1), the Curie constant per Co^{2+} is 3.42 cm^3 K mol^{-1}, which includes the Co^{2+} sites of the β-$Co(OH)_2$, Co_3O_4, and Co_2SiO_4 phases (implying an average g factor of 2.70; it is worth mentioning that Co^{3+} are diamagnetic metal ions). Upon decreasing the temperature, the χT product slightly decreases down to 50 K, indicating dominant AF interactions (right part of Figure S4). The maximum of the χT product at 8.2 K (inset of Figure S4, right part) and the ZFC/FC data below 5 K (inset of Figure S5, left part) confirm the presence of the superparamagnetic β-$Co(OH)_2$ nanoparticles as already observed in MUB-100(1) and MUB-100(2). In the χT versus T data shown in Figure S4 (right part), a clear anomaly at 45 K is observed, which is likely reminiscent of the antiferromagnetic order expected in bulk Co_3O_4.[42] In the same temperature range, the ZFC/FC data in Figure S5 (left part) show also a bifurcation point suggesting the presence of a magnetization blocking typical of superparamagnetic Co_3O_4 nanoparticles.[43] The M versus H data at 2 K, shown in the right part of Figure S5, exhibits a hysteresis loop with a coercive field of 500 Oe, similar to that observed for MUB-100(1) and MUB-100(2) and in agreement with the blocking of the β-$Co(OH)_2$ nanoparticles. At 2 K, the remnant magnetization is 0.010 μ_B while the magnetization value at 9 T is 0.132 μ_B, which corresponds to 1.59 μ_B per Co^{2+} ion (inset of Figure S5, right part). The magnetic properties of MUB-100(3) are similar to those measured for MUB-100(1) and MUB-100(2), indicating a predominant β-$Co(OH)_2$ phase. The $1/\chi$ versus T plot is linear above 50 K and can be fitted to a Curie−Weiss law with C = 0.0994 cm^3 K mol^{-1} and θ = +11.4 K (left part of Figure S4). This material is thus paramagnetic with dominant ferromagnetic interactions between spin carriers. The maximum of the χT product at 8.2 K, the divergence of the ZFC/FC data below 5 K (Figure S5 left part; at 0.4 K/min), and the hysteresis of the M versus H plot (with a coercive field of 810 Oe at 0.2 T/min; Figure S5 right part) confirm the presence of the superparamagnetic β-$Co(OH)_2$ nanoparticles. No clear magnetic signature of the Co_3O_4 phase (i.e., bifurcation on the ZFC/FC data around 45 K as seen for MUB-100(4)) is observed. Nevertheless, considering only the presence of the β-$Co(OH)_2$ phase (i.e., only Co^{2+} ions), the Curie constant per Co^{2+} site is surprisingly low, around 2.21 cm^3 K mol^{-1} (implying an average g factor of 2.17). Taking into account the presence of few percent of Co^{3+} diamagnetic metal ions and the Co^{2+} metal ions from the β-$Co(OH)_2$, Co_3O_4, and Co_2SiO_4 phases as reported in Table 1, the Curie constant per Co^{2+} reaches 2.50 cm^3 K mol^{-1} (implying an average g factor of 2.31) and becomes more reasonable based on previously reported systems. At 2 K, the remnant magnetization is 0.014 μ_B while the magnetization value at 9 T is 0.072 μ_B corresponding to 1.81 μ_B per Co^{2+} ion. It is worth noting that the presence of the Co_2SiO_4 phase is not confirmed by the magnetic measurements on these four samples. For MUB-100(3) and MUB-100(4), this apparent discrepancy is indeed well explained by the extremely small quantity of the Co_2SiO_4 phase detected by other physical characterizations (Table 1). To summarize, the chemical compositions given in Table 1 with the presence of the different magnetic phases, β-$Co(OH)_2$, Co_3O_4, and Co_2SiO_4, are qualitatively and quantitatively coherent with the reported magnetic measurements.

3.4. CO Oxidation through Heterogeneous Catalysis.

The catalytic performances of the MUB-100 series were investigated toward the oxidation of carbon monoxide with oxygen. Carbon monoxide is a colorless, odorless, tasteless, and nonirritating gas for humans and is hard to detect; in addition, it is an intrinsically poisonous gas to all air-breathing organisms because of its high affinity with hemoglobin. The catalytic CO

https://doi.org/10.1021/acsanm.2c01258
ACS Appl. Nano Mater. 2022, 5, 7331−7343

transformation toward CO_2 is a very important reaction involved in several remediation processes, such as in automotive and residential air-cleaning technologies, gas masks for firefighters, CO detectors, selective oxidation of CO in reformer gas for fuel cell applications, and so forth.[44,45] Commercial catalysts dedicated toward CO oxidation are mainly constituted of noble metals, which remain too expensive to be extended at low-cost. Therefore, more attention is dedicated toward harvesting efficient and less-expensive catalysts.

The CO oxidation reaction toward CO_2 is based on a competitive mechanism of adsorption on the active sites between the CO and O_2 molecules.[46] In this study, the CO/O_2 ratio used was equal to 0.4, corresponding to a value allowing work in appropriate experimental conditions. Indeed, for this reaction, the O_2 adsorption at the surface of the catalysts is known to be much weaker than the CO one. Consequently, even with a low CO/O_2 ratio, the active sites are not blocked by the presence of a higher quantity of O_2 molecules.[47] In addition, an excessive CO concentration in the feed gaseous mixture may cause a lower catalytic performance by hindering both the adsorption and dissociation of active O_2 molecules. Figure 7 displays the catalytic performances of the four MUB-100 materials during the CO oxidation as a function of the reaction temperature. The results are presented in terms of CO conversion (Figure 7, left part) or specific activity (Figure 7, right part) expressing the quantity of CO converted to CO_2 per second divided by the mass of Co (active species) contained in the evaluated sample ($mmol_{(CO)} \cdot g_{(Co)}^{-1} \cdot s^{-1}$).

Among the four catalysts, only the MUB-100(4) was able to totally convert the CO before 500 °C under the experimental conditions used, achieving 50% conversion for a light-off temperature T_{50} of 145 °C. This T_{50} value reveals a high efficiency for the MUB-100(4) in CO oxidation, because catalysts presenting similar composition (10 wt %Co/SiO_2) were found to be much less active in the literature. For instance, Lima et al. prepared two Co/SiO_2 catalysts (with 10 wt %) by sol−gel one pot (Op) and impregnation (Im) methods and obtained T_{50} values around 425 °C (Op sample) and 270 °C (Im sample) under operating conditions similar to the ones used here.[48] With a 12 wt %Co/SBA-15 catalyst generated by infiltration of cobalt acetate on sol−gel-based SBA-15 material, Kuboňová et al.[49] observed a T_{50} temperature of 164 °C under experimental conditions more propitious because they used a feed containing 0.1 mol %CO with WHSV = 60 000 $L \cdot h^{-1} \cdot kg^{-1}$ compared in this study to 11.6 mol %CO with WHSV = 120 000 $L \cdot h^{-1} \cdot kg^{-1}$. Several authors have reported that generally Co-silica materials give poor performances in CO oxidation, in contrast to Co-alumina or Co-titania, because of the weak interactions existing between silica and cobalt oxide leading to the sintering of Co species during the thermal treatment.[17,50] The synthetic path used in this study to design the $CoOx-SiO_2$(HIPE) macro-mesocellular (MUB-100) catalysts seems efficient to maintain the high dispersion of the cobalt species while ensuring a high accessibility to the active sites. Indeed, the "one-pot" synthetic path operating at low pH will promote a silica network with a fractal character that favors cobalt oxide nucleation events versus their growth, implying the tendency of generating nanocrystals. As "one-pot" syntheses, the native nanocrystals are embedded within the silica network but still accessible through the mesoscopic voids. Beyond, the presence of a noticeable quantity of Co_3O_4 nanoparticles in the MUB-100(4) sample can also contribute to explain its high conversion. This spinel structure is considered as the most active of the three cobalt oxides CoO, Co_2O_3, and Co_3O_4.[51−53] To corroborate this point, the MUB-100(4) sample was reduced under hydrogen flow as follows: MUB-100(4) sample was placed in a cylindrical furnace and pure H_2 was introduced until reaching a pressure of 2 bar. The sample was then vacuumed for 3 min. This process was repeated 3 times to ensure the lowest O_2 content in the furnace. Then, the sample was submitted to a pure hydrogen flow (with a slight over pressure of 1.05 bar), and the temperature was increased to 400 °C at 10 °C min^{-1}. After 1 day, the sample was cooled to room temperature still under H_2 flow. When the temperature reached 50 °C, the hydrogen flow was stopped while maintaining the pressure at 1.05 bar. The reduced MUB-100(4) material being now amorphous (Figure S6) was then evaluated for CO oxidation (Figure S7), revealing a decrease of the catalytic performances for CO oxidation. The TPR profile obtained during the reduction process (reported in Figure S8) shows that the reduction of the oxidized species occurs in a temperature range between 330 and 430 °C, and the maximum of the consumption peak is located at 384 °C. This peak is generally associated with the reduction of Co_3O_4 species to CoO.[52−55] Actually, the H_2 consumption deduced from the TPR profile (489 μmol $H_2 \cdot g^{-1}$(catalyst)) appears in good agreement with the quantity necessary to reduce all the Co_3O_4 phase contained in the MUB-100(4) sample considering the stoichiometry given in Table 1 and following the reduction reaction

$$Co_3O_4 + H_2 \rightarrow 3CoO + H_2O \quad (2)$$

The absence of a second peak on the TPR profile for the reduction of Co^{2+} to Co^0 can be linked to the formation of cobalt silicate species, stabilizing the +II oxidation state because of Co species in strong interaction with the silica support, which generally requires a higher temperature (>600 °C) to be reduced.[48] Consequently, it seems that the reduction of the Co_3O_4 phase is unfavorable to the catalytic performance. The catalytic experiments being performed with the same mass of catalyst (50 mg) whatever the MUB-100 sample, it is logical that for a given temperature, the CO conversion in Figure 7 (left) evolves accordingly with the Co content in the following order: MUB-100(4) > MUB-100(3) > MUB-100(2) > MUB-100(1). One may argue that this effect is due to lowering the material's intrinsic heat capacities while increasing the Co content. However, this is not the case when considering Figure S9; we can notice that whatever the temperature range the material heat capacities evolve as follows: MUB-100(4) ≈ MUB-100(3) > MUB-100(2) > MUB-100(1). In addition, the specific activity calculated from the conversion values allows comparing the performances of the four MUB-100 samples on the basis of the same Co mass. It must be emphasized that for conversion values reaching 100% (case of the MUB-100(4) material), the calculation of the specific activities per gram of Co is underestimated because the mass of Co present in the sample exceeds necessarily the quantity needed to totally convert the CO molecules. The results given in Figure 7 (right) show that the MUB-100(3), MUB-100(2), and MUB-100(1) materials do not convert CO before 275−300 °C (compared to 125 °C in the case of MUB-100(4)). For these samples, the CO conversion remains below 20% but between 325 and 400 °C. Finally, the specific activities of the less loaded catalyst (MUB-100(1)) are in general superior to the ones displayed by MUB-100(2) and MUB-100(3), indicating

https://doi.org/10.1021/acsanm.2c01258
ACS Appl. Nano Mater. 2022, 5, 7331−7343

the presence of a higher active species content in this sample, probably resulting from a better dispersion of the cobalt entities. Despite the presence of a Co_3O_4 phase on the MUB-100(3) material, this sample displays a specific activity higher than those of the MUB-100(1) and MUB-100(2) catalysts only after 450 °C, indicating that the quantity of Co species involved in this Co_3O_4 phase remains too limited here.

Finally, the catalyst's thermodynamic stabilities have been verified under cycling (Figure S10), indicating a very minimal evolution of the catalytic performance of the MUB-100(4) material during four consecutive cycles of CO oxidation (the catalyst did not undergo any heat treatment between each cycle).

4. CONCLUSIONS

Through the integrative chemistry synthetic path,[56] we have combined sol−gel chemistry, lyotrope mesophases, and direct emulsions to generate the first mixed oxides CoOx−SiO_2(HIPE) macro−mesocellular monolithic materials, labeled MUB-100(x). These multiscale-porous catalysts exhibit a porosity around 95%. At the mesoscopic length scale, the void organization is biphasic vermicular-hexagonal 2D, where the hexagonal 2D is retained further after calcination at 700 °C while increasing the cobalt concentration during the material formulation. The materials depict surface areas between 400 and 500 $m^2\ g^{-1}$ assessed through Ar physisorption investigations. For the lowest cobalt concentrations MUB-100(1) and MUB-100(2), magnetism measurements reveal the β-$Co(OH)_2$ nature of the nanocrystals embedded within the silica matrix while the XRD patterns depict an amorphous character. Considering the mixed oxides bearing the highest cobalt content, the systems is biphasic with both the Co_3O_4 spinel and the Co_2SiO_4 olivine structures. The one-pot synthetic path operates at low pH, promoting thus a silica network with a fractal character. This type of silica network favors cobalt oxide nucleation events versus their growth favoring the generation of nanocrystals, which is true even at the starting silica/cobalt molar ratio of 0.57 for the MUB-100(3) compound. These porous materials have further been tested toward CO oxidation into CO_2. Considering this catalytic application, the MUB-100(4) was able to totally convert the CO flow before 200 °C (starting at 125 °C) while achieving 50% of conversion for a light-off temperature T_{50} of 145 °C, thereby indicating the high efficiency of the MUB-100(4) regarding CO oxidation. On the other hand, we showed that the specific activity normalized per Co mass depicts a crossover where the MUB-100(3), MUB-100(2), and MUB-100(1), which do not convert CO before 275−300 °C, present superior specific activities at high temperature compared to MUB-100(4). We have thus applied hydrogen-based partial reduction to the MUB-100(4) material in order to express further the Co^{2+} species abundance and/or to create an amorphous β-$Co(OH)_2$-based supported catalyst. This material appeared less active than the nonreduced analogue MUB-100(4) material, indicating a lower activity for the CO oxidation of the cobalt(II)-type species compared to the Co_3O_4 phase.

■ ASSOCIATED CONTENT

Supporting Information

The Supporting Information is available free of charge at https://pubs.acs.org/doi/10.1021/acsanm.2c01258.

Thermogravimetric analyses, Porod-like depiction of SAXS, transmission electron nano-diffraction, magnetic susceptibility versus temperature, WAXS of the reduced MUB-100(4), CO conversion (%) versus temperature for MUB-100(4) and reduced MUB-100(4), TPR of the MUB-100(4) material, MUB-100 series heat capacities, and MUB-100(4) effectiveness toward CO-oxidation while cycling (PDF)

■ AUTHOR INFORMATION

Corresponding Authors

Catherine Especel − *Institut de Chimie des Milieux et Matériaux de Poitiers (IC2MP), UMR 7285 CNRS - Université de Poitiers, 86073 Poitiers, France*; Email: catherine.especel@univ-poitiers.fr

Rénal Backov − *Université de Bordeaux, CRPP-UMR CNRS 5031, 33600 Pessac, France*; Email: renal.backov@crpp.cnrs.fr

Authors

Isabelle Ly − *Université de Bordeaux, CRPP-UMR CNRS 5031, 33600 Pessac, France*

Antoine Vardon − *Université de Bordeaux, CRPP-UMR CNRS 5031, 33600 Pessac, France*; orcid.org/0000-0002-3182-5879

Nicolas Chanut − *Department of Civil and Environmental Engineering, Massachusetts Institute of Technology, Cambridge, Massachusetts 02139, United States*

Frédéric Nallet − *Université de Bordeaux, CRPP-UMR CNRS 5031, 33600 Pessac, France*

Roland J.-M. Pellenq − *Department of Civil and Environmental Engineering, Massachusetts Institute of Technology, Cambridge, Massachusetts 02139, United States*

Mathieu Rouzières − *Université de Bordeaux, CRPP-UMR CNRS 5031, 33600 Pessac, France*

Rodolphe Clérac − *Université de Bordeaux, CRPP-UMR CNRS 5031, 33600 Pessac, France*; orcid.org/0000-0001-5429-7418

Joudia Akil − *Institut de Chimie des Milieux et Matériaux de Poitiers (IC2MP), UMR 7285 CNRS - Université de Poitiers, 86073 Poitiers, France*

Florence Epron − *Institut de Chimie des Milieux et Matériaux de Poitiers (IC2MP), UMR 7285 CNRS - Université de Poitiers, 86073 Poitiers, France*; orcid.org/0000-0002-7720-1578

Complete contact information is available at: https://pubs.acs.org/10.1021/acsanm.2c01258

Funding

The authors thank the CNRS and the University of Bordeaux, the Région "Nouvelle Aquitaine", and the Quantum Matter Bordeaux.

Notes

The authors declare no competing financial interest.

■ ACKNOWLEDGMENTS

R.B. thanks Ahmed Bentaleb for acquiring all the SAXS and WAXS data sets, Dr. Marie-Anne Dourges (ISM) for the poro-mercury data acquisitions, Dr. François Dole for acquiring the heat capacities versus temperature, Sabrina Lacomme (Bordeaux Imaging Center- BIC) for the TEM investigations, Dr. François Weill (Placamat-ICMCB) for TEM-TED

investigations. Mr. Eric Lebreau is thanked (ICMCB) for the XRD-investigations. We are thankful to Professor Jean-Louis Bobet (ICMCB) for the MUB-100(4) material H_2 reduction and Ms. Emily Bloch for the MUB-100(3) N_2, Ar physisorption acquisitions (Madirel, Marseille).

REFERENCES

(1) Silverstein, M. S. Recent advances in emulsion-templated porous polymers. *Prog. Polym. Sci.* **2014**, *39*, 199−234.
(2) Silverstein, M. S. Emulsion-templated polymers: Contemporary contemplations. *Polymer* **2017**, *126*, 261−282.
(3) Silverstein, M. S. The Chemistry of Porous Polymers: The Holy Grail. *Israel. J. Chem.* **2020**, *60*, 140−150.
(4) Araya, A. Hydrophobic, Highly Porous, Three-Dimensional Inorganic Structures. US 4888309, 1989.
(5) Carn, F.; Colin, A.; Achard, M.-F.; Deleuze, H.; Sellier, E.; Birot, M.; Backov, R. Inorganic monoliths hierarchically textured via concentrated direct emulsion and micellar templates. *J. Mater. Chem.* **2004**, *14*, 1370−1376.
(6) Brun, N.; Ungureanu, S.; Deleuze, H.; Backov, R. Hybrid foams, colloids and beyond: From design to applications. *Chem. Soc. Rev.* **2011**, *40*, 771−788.
(7) Roucher, A.; Depardieu, M.; Pekin, D.; Morvan, M.; Backov, R. Inorganic, hybridized and living macrocellular foams: "Out of the Box" heterogeneous catalysis. *Chem. Record.* **2018**, *18*, 776−787.
(8) Roucher, A.; Morvan, M.; Pekin, D.; Depardieu, M.; Blin, J.-L.; Schmitt, V.; Baret, J.-C.; Backov, R. From Compartmentalization of Bacteria within Inorganic Macrocellular Beads to the Assembly of Microbial Consortia. *Adv. Biosystems* **2018**, *2*, 1700233.
(9) Brun, N.; Babeau-Garcia, A.; Achard, M.-F.; Sanchez, C.; Durand, F.; Laurent, G.; Birot, M.; Deleuze, H.; Backov, R. Enzyme-Based Biohybrid Foams Designed for Continuous Flow Heterogeneous Catalysis and Biodiesel Production. *Energy Environmental Science* **2011**, *4*, 2840−2844.
(10) Gaikwad, P.; Ungureanu, S.; Backov, R.; Vynck, K.; Vallée, R. A. L. Photon transport in cylindrically-shaped disordered meso-macroporous materials. *Optic Express* **2014**, *22*, 7503−7513.
(11) Bachelard, N.; Gaikwad, P.; Backov, R.; Sebbah, P.; Vallée, R. A. L. Disorder as a Playground for the Coexistence of Optical Nonlinear Effects: Competition between Random Lasing and Stimulated Raman Scattering in Complex Porous Materials. *ACS Photonics* **2014**, *1*, 1206−1211.
(12) Gaikwad, P.; Bachelard, N.; Sebbah, P.; Backov, R.; Vallée, R. A. L. Competition and Coexistence of Raman and Random Lasing in Silica-Titania-Based Solid Foams. *Adv. Optical Mater.* **2015**, *3*, 1640−1651.
(13) Bernadet, S.; Tavernier, E.; Ta, D.-M.; Vallée, R. A. L.; Ravaine, S.; Fécant, A.; Backov, R. Bulk Photo-Driven CO_2 Conversion through TiO_2@Si(HIPE) Monolithic Macrocellular Foams. *Adv. Funct Mater.* **2019**, *29*, 1807767.
(14) Debecker, D. P.; Boissière, C.; Laurent, G.; Huet, S.; Eliaers, P.; Sanchez, C.; Backov, R. First acidic macro-mesocellular aluminosilicate monolithic foams "SiAl(HIPE)" and their catalytic properties. *Chem. Commun.* **2015**, *51*, 14018−14021.
(15) Roucher, A.; Bentaleb, A.; Laurichesse, E.; Dourges, M.-A.; Emo, M.; Schmitt, V.; Blin, J.-L.; Backov, R.; R. First Macro-Mesocellular Silica SBA-15-Si(HIPE) Monoliths: Conditions for Obtaining Self-Standing Materials. *Chem. Mater.* **2018**, *30*, 864−873.
(16) Roucher, A.; Emo, M.; Vibert, F.; Stébé, M.-J.; Schmitt, V.; Jonas, F.; Backov, R.; Blin, J.-L. Investigation of mixed ionic/nonionic building blocks for the dual templating of macro-mesoporous silica foams. *J. Colloid Interface Sci.* **2019**, *533*, 385−400.
(17) Royer, S.; Duprez, D. Catalytic Oxidation of Carbon Monoxide over Transition Metal Oxides *Chem. Catal. Chem.* **2011**, *3*, 24−65.
(18) Wang, R.; He, H.; Wang, J.; Liu, L.; Dai, H. Shape-regulation: An effective way to control CO oxidation activity over noble metal catalysts. *Catal. Today* **2013**, *201*, 68−78.
(19) Kamiuchi, N.; Haneda, M.; Ozawa, M. CO oxidation over Pt/Ce−Zr oxide catalysts with low content of platinum and cerium components. *Catal. Today* **2013**, *201*, 79−84.
(20) Han, W.; Zhang, P.; Tang, Z.; Lu, G. Low temperature CO oxidation over Pd−Ce catalysts supported on ZSM-5 zeolites. *Process Saf. Environ. Prot.* **2014**, *92*, 822−827.
(21) Salomons, S.; Hayes, R. E.; Votsmeier, M.; Drochner, A.; Vogel, H.; Malmberg, S.; Gieshoff, J. On the use of mechanistic CO oxidations models with a platinum monolith catalyst. *Appl. Catal. B Environ.* **2007**, *70*, 305−313.
(22) Fuchs, S.; Hahn, T.; Lintz, H.-G. The oxidation of carbon monoxide by oxygen over platinum, palladium and rhodium catalysts from 10^{-10} to 1 bar. *Chem. Eng. Process. Process Intensif.* **1994**, *33*, 363−369.
(23) Figueroa, S. J. A.; Newton, M. A. What drives spontaneous oscillations during CO oxidation using O_2 over supported Rh/Al_2O_3 catalysts? *J. Catal.* **2014**, *312*, 69−77.
(24) Alonso, E.; Field, F. R.; Kirchain, R. E. Platinum Availability for Future Automotive Technologies *Environ. Sci. Technol.* **2012**, *46*, 12986−12993.
(25) Liu, W.; Flytzani-Stephanopoulos, M. Transition metal-promoted oxidation catalysis by fluorite oxides: A study of CO oxidation over Cu/CeO_2. *Chem. Eng. J.* **1996**, *64*, 283−294.
(26) Biabani-Ravandi, A.; Rezaei, M.; Fattah, Z. Study of Fe-Co mixed metal oxide nanoparticles in the catalytic low-temperature CO oxidation. *Process Saf. Environ. Prot.* **2013**, *91*, 489−494.
(27) Lukiyanchuk, I. V.; Rudnev, V. S.; Chernykh, I. V.; Malyshev, I. V.; Tyrina, L. M.; Adigamova, M. V. Composites with transition metal oxides on aluminum and titanium and their activity in CO oxidation. *Surf. Coat. Technol.* **2013**, *231*, 433−438.
(28) Kang, M.; Song, M. W.; Lee, C. H. Catalytic carbon monoxide oxidation over CoO_x/CeO_2 composite catalysts. *Appl. Catal. A Gen.* **2003**, *251*, 143−156.
(29) Lin, H.; Chiu, H.; Tsai, H.; Chien, S.; Wang, C. *Catal. Lett.* **2003**, *88*, 169−174.
(30) Song, W.; Poyraz, A. S.; Meng, Y.; Ren, Z.; Chen, S.-Y.; Suib, S. L. Mesoporous Co_3O_4 with Controlled Porosity: Inverse Micelle Synthesis and High-Performance Catalytic CO Oxidation at − 60 °C. *Chem. Mater.* **2014**, *26*, 4629−4639.
(31) Lou, Y.; Ma, J.; Cao, X.; Wang, L.; Dai, Q.; Zhao, Z.; Cai, Y.; Zhan, W.; Guo, Y.; Hu, P.; Lu, G.; Guo, Y. Promoting Effects of In_2O_3 on Co_3O_4 for CO Oxidation: Tuning O_2 Activation and CO Adsorption Strength Simultaneously. *ACS Catal.* **2014**, *4*, 4143−4152.
(32) Ly, I.; Layan, E.; Picheau, E.; Chanut, N.; Nallet, F.; Bentaleb, A.; Dourges, M.-A.; Pellenq, R. J.; Hillard, E. A.; Toupance, T.; Dole, F.; Louërat, F.; Backov, R. Design of Binary Nb_2O_5−SiO_2 Self-Standing Monoliths Bearing Hierarchical Porosity and their Efficient Friedel-Crafts Alkylation/Acylation Catalytic Properties. *ACS Appl. Mater. Interfaces* **2022**, *14*, 13305.
(33) Carretero-Genevrier, A.; Gich, M.; Picas, L.; Gazquez, J.; Drisko, G. L.; Boissiere, C.; Grosso, D.; Rodriguez-Carvajal, J.; Sanchez, C. Soft-Chemistry−Based Routes to Epitaxial α-Quartz Thin Films with Tunable Textures. *Sciences* **2013**, *340*, 827−831.
(34) Zangi, R. Can Salting-in/Salting-out Ions Be Classified as Chaotropes/Kosmotropes? *J. Phys. Chem. B* **2010**, *114*, 643−650.
(35) Poyraz, A. S.; Dag, Ö. Role of Organic and Inorganic Additives on the Assembly of CTAB-P123 and the Morphology of Mesoporous Silica Particles. *J. Phys. Chem. C* **2009**, *113*, 18596−18607.
(36) Brinker, C. J.; Scherer, G. W. Sol-Gel Science. In *The Physics and Chemistry of Sol-Gel Processing*; Academic Press, 1990; pp 1−912.
(37) G. Porod, G. In *Small Angle X-ray Scattering*; Glatter, O., Kratky, O.; Academic Press: London, 1982; Chapter 2, pp 17−51.
(38) Lisboa-Filho, P. N.; de Almeida, M. R. C.; Gallo, P. L.; Azevedo, E.; Paskocimas, C. A.; Longo, E.; Ortiz, W. A. Magnetic phases of imperfectly crystalline Co_2SiO_4. *J. Non-Cryst. Solids* **2000**, *273*, 277−281.
(39) Nguyen, P. Q. H.; Zhang, D.; Rapp, R.; Bradley, J. P.; Dera, P. Room temperature facile synthesis of olivine-Co_2SiO_4 nanoparticles

https://doi.org/10.1021/acsanm.2c01258
ACS Appl. Nano Mater. 2022, 5, 7331−7343

utilizing a mechanochemical method. *RSC Adv.* **2021**, *11*, 20687−20690.
(40) Takada, T.; Bando, Y.; Kiyama, M.; Miyamoto, H.; Sato, T. The Magnetic Property of β-$Co(OH)_2$. *J. Phys. Soc. Jpn.* **1966**, *21*, 2726−2726.
(41) Carlin, R. L. In *Magnetochemistry*; Springer: Berlin, 1986; pp 1−328.
(42) Li, H. B.; Liu, P.; Liang, Y.; Xiao, J.; Yang, G. W. Amorphous cobalt hydroxide nanostructures and magnetism from green electrochemistry. *RSC Adv.* **2013**, *3*, 26412−26417.
(43) Dutta, P.; Seehra, M. S.; Thota, S.; Kumar, J. A comparative study of the magnetic properties of bulk and nanocrystalline Co_3O_4. *J. Phys.: Condens. Matter* **2008**, *20*, No. 015218.
(44) Taylor, S. H.; Hutchings, G. J.; Mirzaei, A. A. Copper zinc oxide catalysts for ambient temperature carbon monoxide oxidation. *Chem. Commun.* **1999**, *15*, 1373−1374.
(45) Pillai, U. R.; Deevi, S. Room temperature oxidation of carbon monoxide over copper oxide catalyst. *Appl. Catal. B Environ.* **2006**, *64*, 146−151.
(46) Lou, Y.; Wang, L.; Zhao, Z.; Zhang, Y.; Zhang, Z.; Lu, G.; Guo, Y.; Guo, Y. Low-temperature CO oxidation over Co_3O_4-based catalysts: significant promoting effect of Bi_2O_3 on Co_3O_4 catalyst. *Appl. Catal. B Environ.* **2014**, *146*, 43−49.
(47) Iablokov, V.; Barbosa, R.; Pollefeyt, G.; Van Driessche, I.; Chenakin, S.; Kruse, N. Catalytic CO Oxidation over Well-Defined Cobalt Oxide Nanoparticles: Size-Reactivity Correlation. *ACS Catal.* **2015**, *5*, 5714−5718.
(48) Lima, T. M.; Castelblanco, W. N.; Rodrigues, A. D.; Roncolatto, R. E.; Martins, L.; Urquieta-González, E. A. CO oxidation over Co-catalysts supported on silica-titania−The effects of the catalyst preparation method and the amount of incorporated Ti on the formation of more active Co^{3+}species. *Appl. Catal. A Gen.* **2018**, *565*, 152−162.
(49) Kuboňová, L.; Peikertová, P.; Kutláková, K. M.; Jirátová, K.; Slowik, G.; Obalová, L.; Cool, P. Catalytic activity of cobalt grafted on ordered mesoporous silica materials in N_2O decomposition and CO oxidation. *Mol. Catal.* **2017**, *437*, 57−72.
(50) Neha; Prasad, R.; Vir Singh, S. Catalytic abatement of CO, HCs and soot emissions over spinel-based catalysts from diesel engines: An overview. *J. Environ. Chem. Eng.* **2020**, *8*, 103627.
(51) Wang, C. B.; Tang, C. H.; Tsai, H. C.; Chien, S. H. Characterization and Catalytic Oxidation of Carbon Monoxide over Supported Cobalt Catalysts. *Catal. Lett.* **2006**, *107*, 223−230.
(52) Dey, S.; Dhal, G. C. The catalytic activity of cobalt nanoparticles for low-temperature oxidation of carbon monoxide. *Mater. Today Chem.* **2019**, *14*, 100198.
(53) Rosynek, M. P.; Polansky, C. A. Effect of cobalt source on the reduction properties of silica-supported cobalt catalysts. *Appl. Catal., A* **1991**, *73*, 97−112.
(54) Jacobs, G.; Chaney, J. A.; Patterson, P. M.; Das, T. K.; Davis, B. H. Fischer−Tropsch synthesis: study of the promotion of Re on the reduction property of Co/Al_2O_3 catalysts by in situ EXAFS/XANES of Co K and Re L_{III} edges and XPS. *Appl. Catal., A* **2004**, *264*, 203−212.
(55) Eschemann, T. O.; Oenema, J.; de Jong, K. P. Effects of noble metal promotion for Co/TiO_2 Fischer−Tropsch catalysts. *Catal. Today* **2016**, *261*, 60−66.
(56) Backov, R. Combining soft matter and soft chemistry: integrative chemistry towards designing novel and complex multiscale architectures. *Soft Matter.* **2006**, *2*, 452−464.

https://doi.org/10.1021/acsanm.2c01258
ACS Appl. Nano Mater. 2022, 5, 7331−7343